Journal of
Ceramic Science
and Technology

J. Ceram. Sci. Tech., 07 [02] 155-164 (2016)
DOI: 10.4416/JCST2015-00081
available online at: http://www.ceramic-science.com

Thermal Shock and Thermo-Mechanical Behavior of Carbon-Reduced and Carbon-Free Refractories

A. Böhm[1], S. Dudczig[2], J. Fruhstorfer[2], A. Mertke[2], C.G. Aneziris[2], J. Malzbender[*1]

[1]Forschungszentrum Jülich GmbH, Institute of Energy and Climate Research, IEK - 2, Wilhelm-Johnen-Strasse, D-52425 Jülich, Germany
[2]TU Bergakademie Freiberg, Institute of Ceramic, Glass and Construction Materials, Agricolastraße 17, D-09596 Freiberg, Germany

received December 4, 2015; received in revised form February 1, 2016; accepted February 20, 2016

Abstract

The thermal shock behaviour of novel carbon-reduced refractories with maximum grain size of 1 mm was investigated. A wedge splitting test for small specimen geometries (max. 40 × 40 × 20 mm^3) was successfully implemented with different loading configurations to determine "work of fracture" and thermal shock parameters. Additionally, heating-up thermal shock tests were performed with an electron beam facility. The addition of 2.5 wt% ZrO_2 and TiO_2 to Al_2O_3 refractories appears to improve their thermal shock resistance due to microstructural changes that reduce brittleness and inhibit critical crack growth. However, a phase transition of ZrO_2 affects the properties at elevated temperature. For another pure alumina refractory, no geometry-independent value for the work of fracture could be obtained for the sample geometry used, which is probably related to the formation of a large interaction zone of the fracture surfaces. Al_2O_3-C materials with addition of semi-conductive Si and nanoparticles revealed a strong effect of the pressing direction on the work of fracture. However, the thermal shock parameter R'''' was hardly affected by the different additives. Furthermore, thermal shock tests using the electron beam facility JUDITH 1 did not indicate any significant differences in the damage pattern of the different Al_2O_3-C materials.

Keywords: Ceramics, refractories, thermal shock, wedge splitting test, electron beam

I. Introduction

Thermal shock resistance is one of the key properties of refractories, since linings and components have to withstand fast temperature changes during charging, tapping and casting processes[1]. The use of carbon increases the thermal shock resistance of refractories. However, a reduction of carbon results in better insulating properties and reduced carbon pick-up of the steel. The development of a new generation of carbon-free and carbon-reduced refractories for steel applications with excellent thermal shock resistance has been the aim of the SPP 1418 – "FIRE" program.

In order to characterize thermal shock behavior, different approaches have been developed, applying analytical and phenomenological methodologies[2]. Based on the fracture mechanics of brittle ceramics, Hasselman[3, 4] derived several thermal shock parameters, also called "figures of merit". The most important parameters for the characterization of thermal shock damage are:

$$R'''' = \frac{\gamma_{WOF} \times E}{\sigma_f^2} \quad (1)$$

as well as

$$R_{st} = \sqrt{\frac{\gamma_{WOF}}{E \times a^2}} \quad (2)$$

with E being the Young's modulus, σ the fracture stress, γ_{wof} the work of fracture and α the thermal expansion coefficient. R'''' represents the resistance against kinetic crack growth, while R_{st} is proportional to the critical temperature for crack propagation.

An accurate determination of γ_{wof} is the most important basis for the calculation of R'''' and R_{st}. However, owing to the typically heterogeneous microstructure of refractories, necessary sample geometries have to differ from the ones used for structural ceramics.

Refractory materials are usually able to accumulate large amounts of elastic energy before crack initiation, however, the sum of elastic energy stored in the sample and testing machine should be quite low in order to avoid catastrophic failure. The wedge splitting test (WST) after Tschegg[5, 6] (Fig. 1a) fulfills the necessary requirements and is therefore a commonly used method for testing the fracture behavior of refractories and other quasi-brittle materials[7, 8, 9]. Fig. 1 illustrates schematically the experimental set-up and suggested specimen geometry. A vertical load is applied via a wedge and transformed into horizontal load by a loading transmission device. Notch opening can be measured using an extensometer. The influence of friction is negligible and horizontal force F_H can be calculated from the vertical load F_V and the angle of the wedge β:

$$F_H = \frac{F_V}{2\tan(\frac{\beta}{2})} \quad (3)$$

* Corresponding author: j.malzbender@fz-juelich.de

The work of fracture can be calculated from the load-displacement data if crack propagation is stable during the entire splitting process:

$$\gamma_{WOF} = \frac{1}{2A}\int_0^{\delta_{H,max}} F_H d\delta_H \quad (4)$$

where δ_H is the horizontal displacement (notch opening at the load line) and A the ligament area (A is multiplied by 2 since two new surfaces are created).

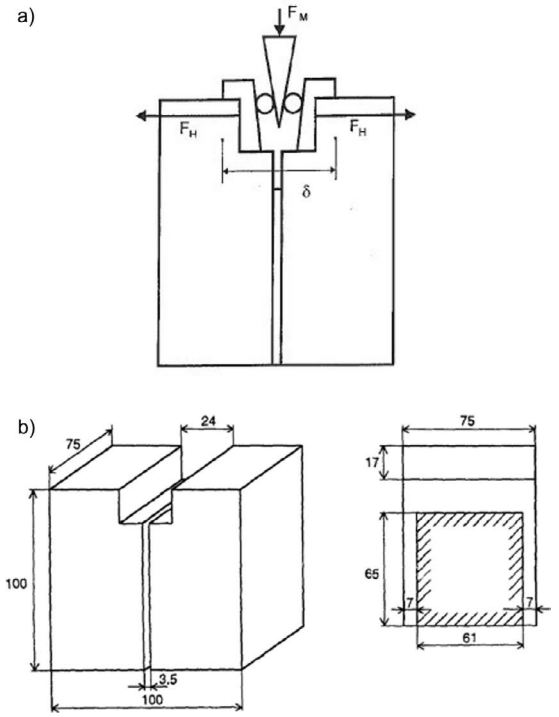

Fig. 1: a) Experimental set-up for WST after Tschegg[6]; b) Suggested specimen geometry for the WST after Tschegg[6].

Phenomenological methods to describe thermal shock performance are mostly based upon rapid quenching of heated samples (e.g. thermal shock by water quenching[10]). Thermal shock behavior is evaluated based on microscopic assessment of the damage, comparing Young's modulus or fracture stress before and after thermal shock or counting thermal shock cycles until failure occurs[10]. However, in application, severe thermal shocks are induced by fast heating not as a result of cooling and hence, cooling-derived thermal shock does not result in the same thermal stress distribution in a sample as a heating-derived thermal shock and will therefore most probably not lead to the same damage pattern.

A promising novel approach to investigate the heating thermal shock behavior of refractories is the application of an electron beam in order to produce short and strong thermal shocks, while avoiding chemical interaction with steel or slag. So far this method has been established to characterize thermal shock behavior of first wall materials for fusion power plants (e.g. Linke *et al.*[11, 12]). Initial tests on refractory materials have been conducted by Skiera *et al.*[13]. However, it was observed that erosion was the main damage mechanism; long cracks or crack networks could not be observed.

The current work focuses on thermo-mechanical characterization of carbon-free and carbon-reduced refractories within the framework of the SPP 1418 – "FIRE" program. Besides thermo-mechanical characterization, the development and optimization of testing methods was a focus of this study. A new WST set-up for small specimen geometries with different loading configurations has been implemented at Forschungszentrum Jülich, permitting also elevated temperature tests up to 1000 °C. Additionally, thermal shock tests were conducted using the electron beam test facility JUDITH 1. Different Al_2O_3-based materials were investigated. Al_2O_3 exhibits very good corrosion resistance but has a poor thermal shock performance[14]. One approach to improve thermal shock resistance is the addition of ZrO_2 and TiO_2 (AZT)[15]. Owing to the formation of Al_2TiO_5 during sintering and its accompanied volume increase, a micro-crack network is formed. Moreover, the different phases (zones) reveal different thermal expansion coefficients and form the so-called spring elements that contribute to improved thermal shock resistance[16]. The investigated AZT material represents the state of the art at the beginning of the SPP-1418 – "FIRE" program. Al_2O_3 was investigated as the state-of-the-art reference material, whereas the alumina material is a reference for a newer series of AZT materials, however, on account of the very low strength of these AZT materials, specimens for WST and CT tests could not be prepared.

Another approach for the reduction of carbon in refractories is the addition of semi-conductive Si and/or nanoparticles. The use of semi-conductive Si can result in higher carbon content after coking and therefore enhances thermal shock resistance[17]. Nanoparticles (e.g. alumina sheets, carbon nanotubes) are able to improve thermal shock performance as well. Owing to their high reactivity, the formation of whisker networks is enhanced. Interlocking of these whiskers leads to higher strength of refractories[18]. Additionally, heating can cause healing or reformation of whiskers, which enhances thermal shock resistance[19]. Hence, in this study Al_2O_3-C materials without additives (A-C, reference), with additions of semi-conductive Si (A-C-Si) and with additions of semi-conductive Si, alumina nano-sheets and carbon nanotubes (A-C-Si-TNAS) were investigated.

II. Experimental

The investigated materials were developed at TU Freiberg in three different projects within the Priority Program (AN322/15 – 1, AN 322/27 – 1, AN322/16 – 2). Compositions are listed in Table 1 and Table 2. Details of the raw materials, grain size distribution and production procedure can be found in Skiera *et al.*[20] (Al_2O_3/AZT), Böhm *et al.*[21] (alumina) and Merkte and Aneziris[22] (Al_2O_3-C; investigated materials were produced according to curing condition 2).

Work of fracture determination and *in-situ* crack propagation observations were carried out using a new WST set-up developed within the framework of the Priority Program at Forschungszentrum Jülich GmbH. Samples with maximum grain of 1 mm were investigated. The small maximum grain size compared to typical refractory materials allows a reduction of specimen geometry ($20 \times 20 \times 20$ mm^3 – $40 \times 40 \times 20$ mm^3) and therefore enables a larger number of tests in a particular time interval.

Moreover, tests with small specimens (20 × 20 × 20 mm³) could be carried out in an SEM chamber for detailed crack propagation observations (details can be found in Skiera *et al.* [20]). The reduced specimen geometry excluded the application of the loading transmission device suggested by Tschegg. Hence, in the current work two different loading configurations were used:

1. Direct contact between sample and wedge (Fig. 2a).
2. Fixed rollers in a groove (Fig. 2b).

Table 1: Composition of tested carbon-free refractories.

Raw materials	Compositions wt %		
	Al_2O_3 (A)*)	AZT*)	Alumina**)
Al_2O_3	100	95	100
ZrO_2	-	2.5	-
TiO_2	-	2.5	-
*) Materials with maximum grain size of 1 mm (A1 and A1AZT) or 200 µm (A200 and A200AZT) were produced. **) Maximum grain size 1 mm			

Table 2: Composition of tested carbon-reduced refractories.

Raw materials	Compositions wt %		
	A-C	A-C-Si	A-C-Si-TNAS
Al_2O_3*)	58	58	58
C	20	20	20
Si	6	5.5	5.5
Novolac liquid	4	4	4
Novolac powder	2	2	2
Si (semiconductive)	-	0.5	0.5
Carbon nanotubes	-	-	0.3
Alumina nanosheets	-	-	0.1
*) Maximum grain size 0.6 mm			

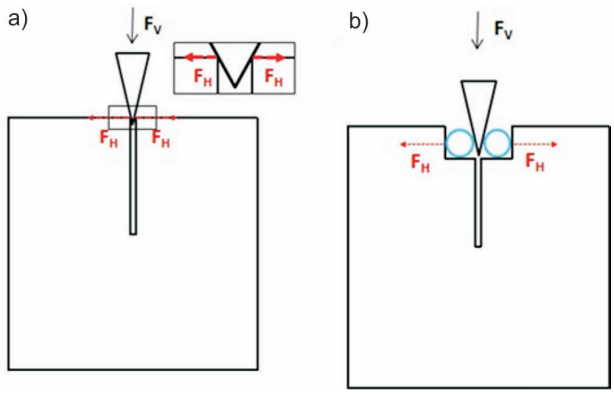

Fig. 2: a) Loading configuration 1; b) Loading configuration 2.

Loading configuration 1 (LC1) was introduced by Skiera *et al.* [20]. The main advantages are the flexibility with respect to sample geometries and the simplicity, also with respect to sample preparation. Within the current study, tests were conducted with sample geometries of 20 × 20 × 20 mm³, 37.5 × 40 × 20 mm³ and 40 × 40 × 20 mm³. For loading configuration 2 (LC2), grooved samples with a geometry of 40 × 40 × 20 mm³ were used. Depth and width of the groove were 5 or 10 mm, respectively, which limits the reduction possibilities with respect to the sample geometry. Rollers with a diameter of 4 mm were used, therefore the load line was at 37 mm. Samples were provided with notch lengths ranging between a/W = 0.4 – 0.75 (a/W = notch length/specimen length, measured from load line to bottom of sample/notch). In both cases, friction cannot be neglected and Eq. 3 has to be extended by a friction influence factor f:

$$f = \frac{1 - \mu \times \tan(\beta/2)}{1 + \mu/\tan(\beta/2)} \tag{5}$$

with μ being the friction coefficient. F_H can then be calculated via:

$$F_H = f \times \frac{F_V}{2\tan(\frac{\beta}{2})} \tag{6}$$

The friction influence factor can be determined by calibrating the load-displacement curves obtained from WST and frictionless compact tension (CT) tests (a more detailed explanation about the experimental set-up can be found in Skiera *et al.* [20]). The CT tests were carried out using the same specimen geometry that was used for WST with LC2, leading to load line at 37.5 mm. Skiera *et al.* [20] determined a friction influence factor f of 0.24 for the Al_2O_3 and AZT samples. Calibration was done via the ratio of $F_{H,Max}$ (maximum horizontal force) obtained from CT tests and WST.

For the Al_2O_3-C samples, the friction influence factor f was determined for LC1 and LC2 via the ratio of notch tensile strength σ_{NT} obtained from CT and WST:

$$\sigma_{NT} = \frac{F_{H,Max}}{B \times L} \times \left(1 + \frac{6 \times \gamma}{L}\right) \tag{7}$$

where B and L are width and length of the ligament and $\gamma = ((W\text{-}a)/2) + a$. The fracture stress was chosen as the parameter for calibration instead of $F_{H,Max}$, in order to reduce inaccuracies resulting from small geometry variations (specimen size and notch length).

Experiments at room temperature were performed using a metal wedge with β = 40° loaded vertically with a crosshead speed of 25 µm/min. The fracture surface A is defined as the product of W-a and the width of the specimen. Crack propagation was monitored using a Basler Camera A 402k equipped with a Nikon telephoto lens and a focal lens of 28 – 200 mm. In order to visualize the crack path, an image correlation software tool was used.

Elevated temperature (HT, up to 1000 °C) experiments were carried out in an Instron testing machine using a ceramic wedge with β = 20°. The friction correction factor (0.21) was determined at RT[23]. Since the notch opening at HT could not be measured directly, a long-distance microscope was used, which recorded 30 images per minute. The notch opening was determined from these images (optical resolution 1.7 µm/pixel), which were synchronized with the vertical force data. The experiments were carried out using a vertically crosshead speed of 25 µm/min.

Powder XRD was used to analyze the phase composition. The measurements were carried out using a D5000 X-ray diffractometer (Siemens, Germany) in the temperature range 25 to 1000 °C.

Thermal expansion was measured in the temperature range 25 to 1000 °C using a horizontal push rod dilatometer (Netzsch Group, Germany). The experiments were conducted in accordance with DIN 51045[24].

An impulse excitation technique was applied to determine the dynamic elastic modulus[25, 26]. With the resonant frequency of the fundamental bending mode (f_f), the elastic modulus of bar-shaped samples can be calculated according to ASTM E 1876 – 01[27]:

$$E = 0{,}9465 \times \left(\frac{m \times f_f^2}{b}\right)\left(\frac{L^3}{t^3}\right)T_1 \qquad (8)$$

where m is the mass of the sample, L the length, b the width and t the height. T_1 is a geometry correction factor. Measurements were performed using a commercial GrindoSonic set-up that permitted tests to be carried out up to 1100 °C (J.W. Lemmens N.V., Belgium). A bar geometry of 45 × 14 × 6 mm^3 was chosen taking into account the limited space of the test set-up, while still ensuring the required height/maximum grain size to length/height ratio of > 5 [27].

Thermal shock tests were conducted with the electron beam facility JUDITH 1 (Juelich Divertor Test Facilities in the Hot Cells). The facility consists of a vacuum chamber (10^{-4} mbar), an electron gun and several devices for data acquisition (pyrometer, cameras with optical and infrared objectives). The electron beam "scans" a pre-defined sample area. The severity of thermal shock can be varied by changing the beam current and/or acceleration voltage. The actual thermal shock temperature was determined by a fast pyrometer along with supporting FEM simulation [23].

III. Results and Discussion

AZT/Al_2O_3

All WST were carried out using LC1 with the friction correction factor of 0.24 determined by Skiera *et al.* [20]. Samples with geometries of 40 ×40 ×20 mm^3 (large), 20 × 20 × 20 mm^3 and 20 × 20 × ~9 mm^3 (small, halved 20 × 20 × 20 mm^3 sample) were investigated. Stable crack growth for A1 samples was only achieved for $a/W = 0.7$. Variation of the ligament area could only be achieved with variation of the sample size. A1AZT materials were successfully tested with $a/W = 0.4 - 0.7$. The data are presented in Fig. 3. Since different sample geometries were used, the ligament area instead of a/W is presented on the x-axis. No size effect could be observed in the case of A1 since the data set is not sufficient owing to the specimen size limitation. In the case of A1AZT-1600-III, work of fracture appears to increase with increasing ligament area, but A1AZT-1650 displays converse behavior. No trend can be observed for A1-AZT-1500 and A1-AZT-1600-II. Comparing these trends with the general overall scattering of the data points, a clear size effect cannot be identified.

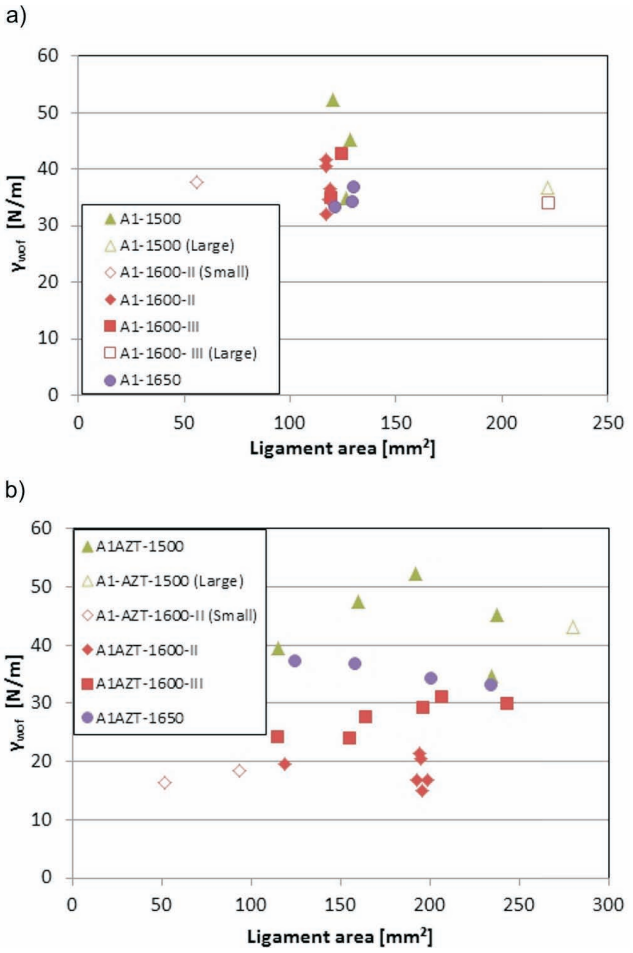

Fig. 3: Work of fracture vs. ligament area of a) A1 b) A1AZT.

Table 3 summarizes the thermal shock parameters obtained from WST at RT. The results include the data published by Skiera[28] and Skiera *et al.* [20]. The improved thermal shock behavior of AZT materials compared to Al_2O_3 is probably related to non-linear effects in the wake zone such as micro-cracking, crack branching and bridging of fracture surfaces [20]. These effects are a result of the complex microstructure, which has been investigated and discussed in more detail in previous studies[29, 30].

Furthermore, a clear effect of the sintering temperature on material properties and the thermal shock parameters can be observed. Fruhstorfer *et al.*[31] reported an effect of the sintering temperature on the formation of Al_2TiO_5 in AZT materials, which has a strong impact on the microstructure. Based on the results reported in this study, a hypothesis has been derived: the formation of Al_2TiO_5 starts at around 1280 °C. This formation is accompanied by an increase in volume and leads therefore to the formation of micro-cracks. This mechanism results in a continuous decrease of Young's modulus and fracture stress with increasing temperature up to sintering temperatures of about 1600 °C, where the formation of Al_2TiO_5 is expected to be completed. The sinter activity increases once the formation of Al_2TiO_5 is completed, which results in an increase in Young's modulus. The observation that the fracture stress does not increase for higher sintering temperatures might be related to both porosity effects as well as pore size distribution.

Table 3: Mechanical properties of A1 and A1AZT at RT.

Sintering temp.	$E^{*)}$	$\sigma^{*)}$	$\alpha_{(RT-1000)}$	γ_{wof}	R''''	R_{st}
°C	GPa	MPa	$10^{-6}\cdot K^{-1}$	N/m	mm	$K\cdot m^{0.5}$
A1						
1500	169 ± 2	81 ± 1	8.28	38.7 ± 3.4	1.0 ± 0.1	1.8 ± 0.1
1600-I	166 ± 2	88 ± 8	8.33	37.2 ± 3.6	0.8 ± 0.1	1.8 ± 0.1
1600-II	166 ± 2	88 ± 8	8.33	37.2 ± 4.8	0.8 ± 0.2	1.8 ± 0.2
1650	189 ± 7	61 ± 13	-	41.8 ± 1.3	2.1 ± 0.1	-
A1AZT						
1500	84 ± 3	21 ± 1	7.81 ± 0.01	41.9 ± 7.1	7.8 ± 1.4	2.8 ± 0.3
1600-I	68 ± 11	14.9 ± 0.4	7.69 ± 0.13	18.1 ± 2.2	5.6 ± 0.7	2.1 ± 0.2
1600-II	68 ± 11	14.9 ± 0.4	7.69 ± 0.13	27.6 ± 3.0	8.5 ± 1.0	2.6 ± 0.2
1650	77 ± 4	14 ± 1	-	35.3 ± 2.0	13.6 ± 0.8	-

*) Determined at TU Bergakademie Freiberg using ultrasonic runtime measurements (E) and 3-point bending tests (σ), respectively.

Another strong effect on the material behavior appears to be the phase transformation of ZrO_2 at elevated temperatures, which was verified by means of XRD investigations (Fig. 4). The reversible transformation of monoclinic (m) ZrO_2 into tetragonal (t) ZrO_2 takes place in a temperature interval from 600 °C to 900 °C. During cooling the transformation is reversed in a temperature interval from 700 °C to 400 °C. Literature reports indicate phase transformation temperatures of > 1000 °C (m→t) and < 950 °C (t→m), respectively[32]. However, the incorporation of TiO_2 lowers the phase transition temperature of ZrO_2. In fact, EDX investigations confirmed the presence of TiO_2 within the ZrO_2 lattice. Comparing the phase transition temperature intervals with data from Pandolfelli *et al.*[33], it can be estimated that the amount of incorporated TiO_2 is between 12 and 18 vol%.

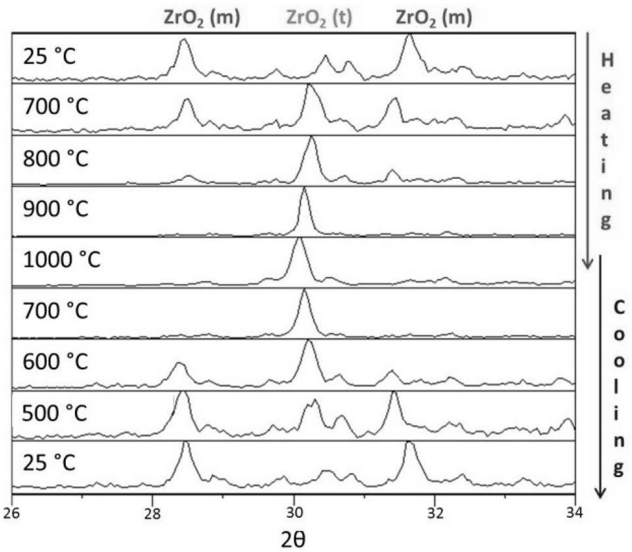

Fig. 4: Excerpt of the HT-XRD pattern an A1AZT-1600 sample.

The phase transformation has a strong impact on the temperature-dependent elastic behavior, i.e. the Young's modulus displayed strong thermal hysteresis (Fig. 5). Young's modulus values of AZT materials at 1000 °C are up to a factor of two higher than at RT. Such behavior has also been reported for Al_2O_3-ZrO_2 refractory materials in other studies[34, 35]. The phase transformation of ZrO_2 is accompanied by a volume change of 3 – 5 %, which can also be seen in dilatometer curves (Fig. 6), and this might lead to debonding and damage owing to thermal expansion mismatch between grains and matrix[36].

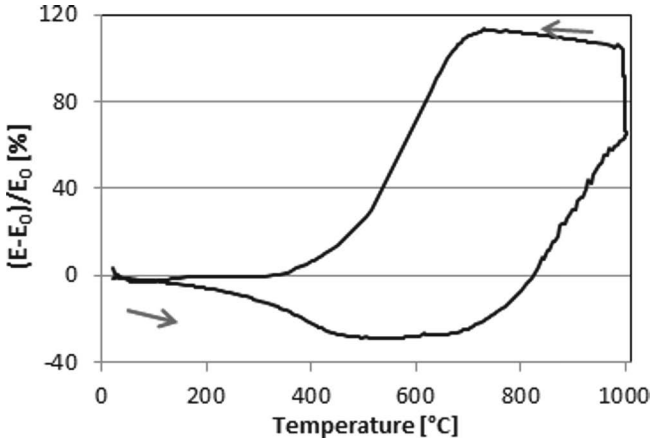

Fig. 5: Relative change of elastic modulus with temperature an A1AZT-1650 sample.

Elevated temperature WST carried out at 800 °C before and after the phase transformation revealed a strong influence of ZrO_2 modification on fracture mechanical behavior. A load-displacement curve obtained at 800 °C before the phase transformation of ZrO_2 (m→t) indicates a similar behavior as at RT (Fig. 7a). A higher value of γ_{wof} results from an increased flexibility (notch opening at 0.1 $F_{H,Max}$) [23]. The presence of tetragonal ZrO_2 in AZT materials leads to an increase in fracture stress (detected based on the increase of $F_{H,Max}$) and a decrease in flexibility. The phase transformation of ZrO_2 (m→t) and the associated

microstructural evolution leads to a more brittle fracture behavior than at RT (Fig. 7b).

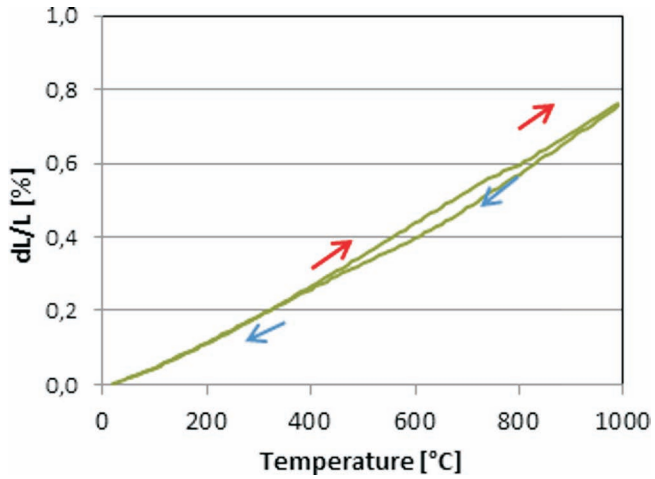

Fig. 6: Dilatometer curve of an A1AZT-1500 sample.

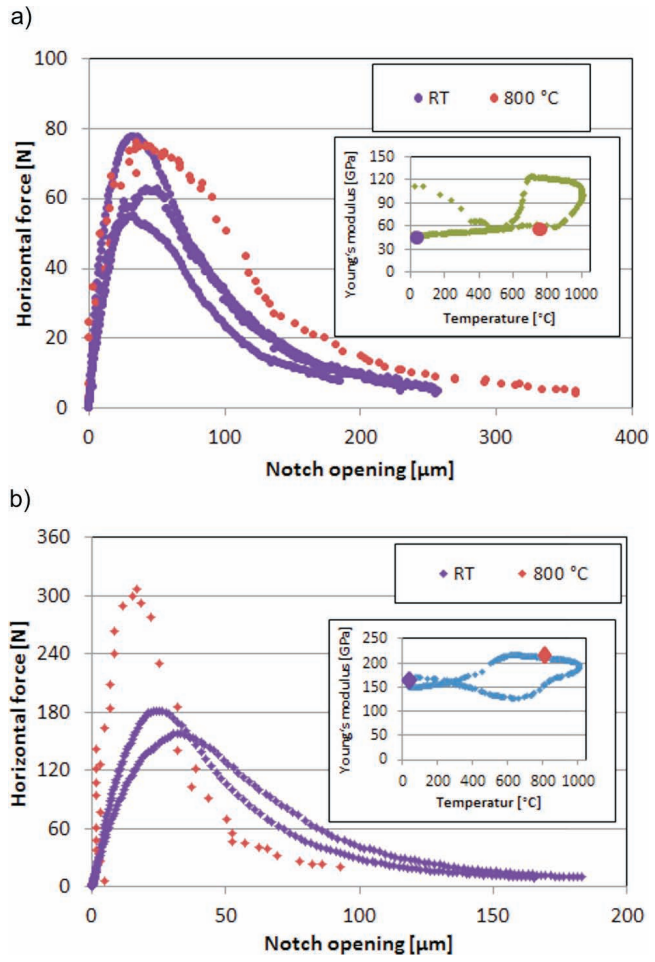

Fig. 7: a) Load-displacement curve from WST of an A200AZT-1600 sample at 800 °C before phase transition of ZrO_2; b) Load-displacement curve from WST of an A200AZT-1500 sample at 800 °C after phase transition of ZrO_2.

Alumina

CT tests and WST with both loading configurations were also performed on alumina materials. Tests with LC1 did not yield stable load-displacement curves (Fig. 8). In particular, the rising part of the load-displacement curves exhibits a discontinuous behavior with a large scattering in $F_{H,Max}$ (and therefore σ_{NT}) even though a/W values were similar, hence resulting in a large scatter of γ_{wof} data. Because of this large scatter, no friction coefficient could be determined. This behavior is assumed to be related to the weak grain bonding of the tested alumina materials. Owing to the direct contact of wedge and sample, mechanical stresses lead to damage at the contact surface and therefore to discontinuities in the sustainable load.

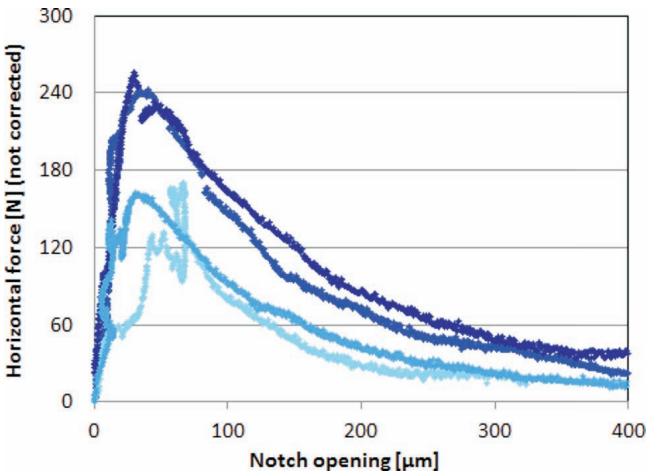

Fig. 8: Load-displacement curves for Alumina materials in LC1.

Tests with LC2 and CT tests revealed stable load-displacement curves. Hence a significant smaller scatter of $F_{H,Max}$ was observed for LC2. Furthermore, the results indicated no significant influence of friction for LC2. The γ_{wof} values obtained from CT tests and WST in case of LC2 are presented in Fig. 9.

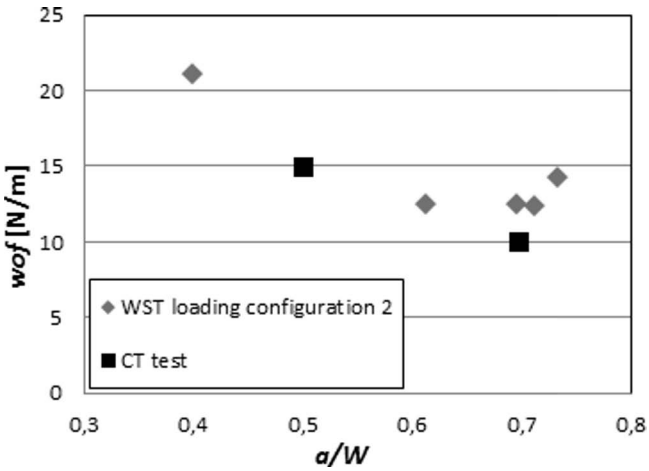

Fig. 9: Dependency of γ_{wof} on the initial notch length for Alumina materials.

Friction coefficients could not be obtained owing to the large scatter of LC1 data. The γ_{wof} data of alumina materials show a clear size effect in the range $a/W = 0.7 - 0.4$. No plateau region could be deduced based on the obtained results. The complete pullout of big grains in the wake zone enlarges the interaction zone of the fracture surfaces. For this material, it seems to be necessary to increase the specimen geometry for WST in future works in order to obtain geometry-independent results.

Al_2O_3-C

Further investigations using different LCs were performed with Al_2O_3-C materials. Owing to the alignment of the graphite flakes parallel to the pressing direction, the WST was performed with samples that were notched parallel and perpendicular to the pressing direction (Fig. 10). Stable load-displacement curves could be obtained in all cases. Friction coefficients were calculated based on Eq. 8, yielding 0.34 (LC1) and 0.13 (LC2), respectively (the friction factor was estimated to have an accuracy of 0.05).

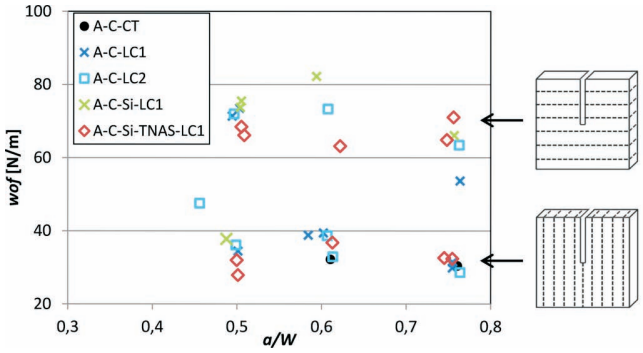

Fig. 10: Dependency of γ_{wof} on the initial notch length for Al_2O_3-C materials for different loading configurations.

The γ_{wof} values obtained from CT tests and WST are presented in Fig. 11. The calculated friction coefficients are higher in the case of LC1. This result was expected since the friction between a rough ceramic surface and the steel wedge is supposed to be higher than friction between two smooth (steel) surfaces. The calculated friction coefficient in the case of LC2 (0.13) agrees with the reported friction coefficient for steel/steel contacts[37].

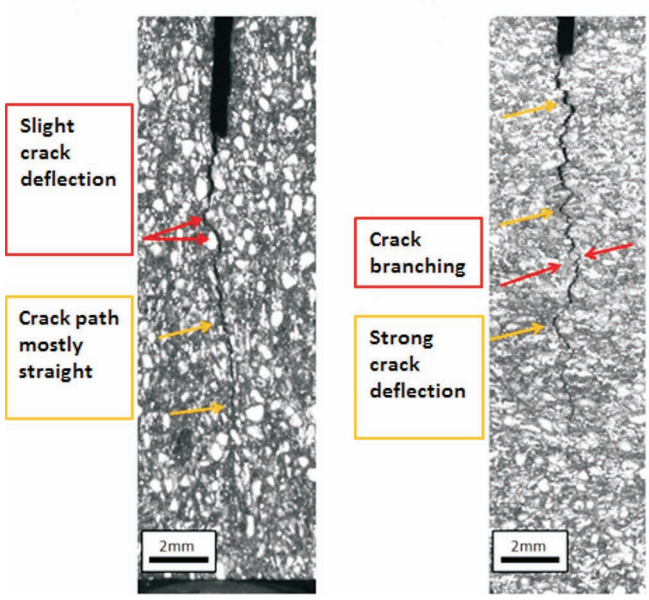

Fig. 11: Crack propagation in Al_2O_3-C samples with notch parallel to pressing direction (left) and notch perpendicular to pressing direction (rigth).

A clear "size-effect" for γ_{wof} was not detected for Al_2O_3-C materials. However, a huge difference in γ_{wof} with respect to the pressing direction was revealed. Specimens with a crack path parallel to the pressing direction showed around 50 % lower values compared to specimens with a crack path perpendicular to the pressing direction. The crack path parallel to the pressing direction was mostly straight, while the crack perpendicular to the pressing direction showed a large number of crack deflections. Hence, in this case the rough surface of the ligament areas leads to frictional effects during crack opening and therefore higher energy consumption.

R'''' was calculated for crack growth perpendicular to the pressing direction (Table 4). The samples with additives revealed a lower value than the reference without additives (A-C). This effect can be related to an increase in strength and Young's modulus, while γ_{wof} stays constant. However, Mertke and Aneziris [22] observed an improvement of the thermal shock resistance with the addition of these additives (data are presented in Table 4). Thermal shock resistance was assessed based on the change in strength after quenching samples with compressed air. The addition of Si or nanoparticles is supposed to support the formation of interlocking whisker networks. These whisker networks are formed at elevated temperatures, which means that reheating might have a healing effect.

Table 4: Mechanical properties of Al_2O_3-C at RT.

	$E^{*)}$	$\sigma^{*)}$	γ_{wof}	R''''
	GPa	MPa	N/m	mm
A-C	12.7 ± 0.2	10.3 ± 0.2	68 ± 4	8,1 ± 1,0
A-C-Si	15.6 ± 2.2	13.2 ± 1.2	74 ± 3	6,6 ± 0,6
A-C-Si-TNAS	18.9 ± 0.3	14.5 ± 0.3	67 ± 5	6,0 ± 0,3

*) Determined at TU Bergakademie Freiberg using ultrasonic runtime measurements (E) and 3-point bending tests (σ), respectively.

Table 5: Operation conditions for thermal shock tests on the Judith 1 electron beam facility.

Condition	Current [mA]	Cycles	Time [ms]	Power density [MW/m²]	Temp. [°C]
1	78	100	100	21.1	1250
2	78	50	200	21.1	1450
3	90	100	100	24.3	1350
4	90	30	100	24.3	1250

Complementary experiments for the Al_2O_3-C materials were carried out on the JUDITH 1 facility. The operation conditions and the maximum temperature (after the last thermal shock cycle) are given in Table 5. Acceleration voltage was 120 kV with a pause of 2 s between every pulse (cycle). Evenly distributed damage was observed for the thermally shocked areas. Thermal shock temperatures up to 1450 °C were realized. The damage was quantified based on the material loss (Fig. 12). For all materials, the highest weight loss was obtained with operation condition 2 (highest thermal shock temperature). Other oper-

ation conditions yielded lower weight losses. SEM images revealed micro-cracks in the grain matrix boundary after thermal shock (Fig. 13). A significant dependence of material loss or damage pattern on the addition of semi-conductive Si and/or nanoparticles was not observed.

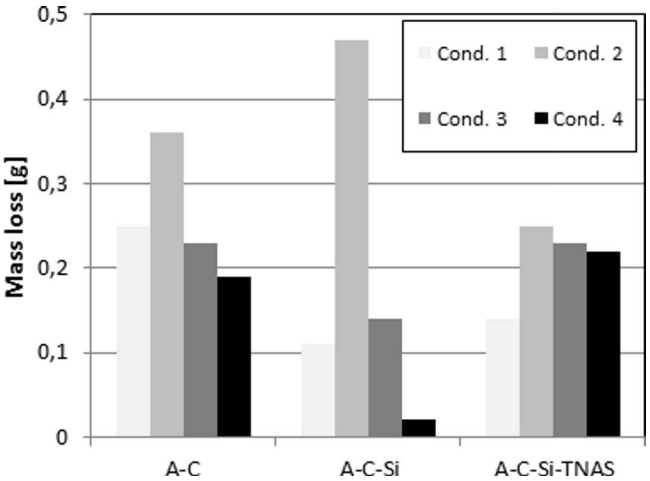

Fig. 12: Material loss of Al_2O_3-C materials after thermal shock.

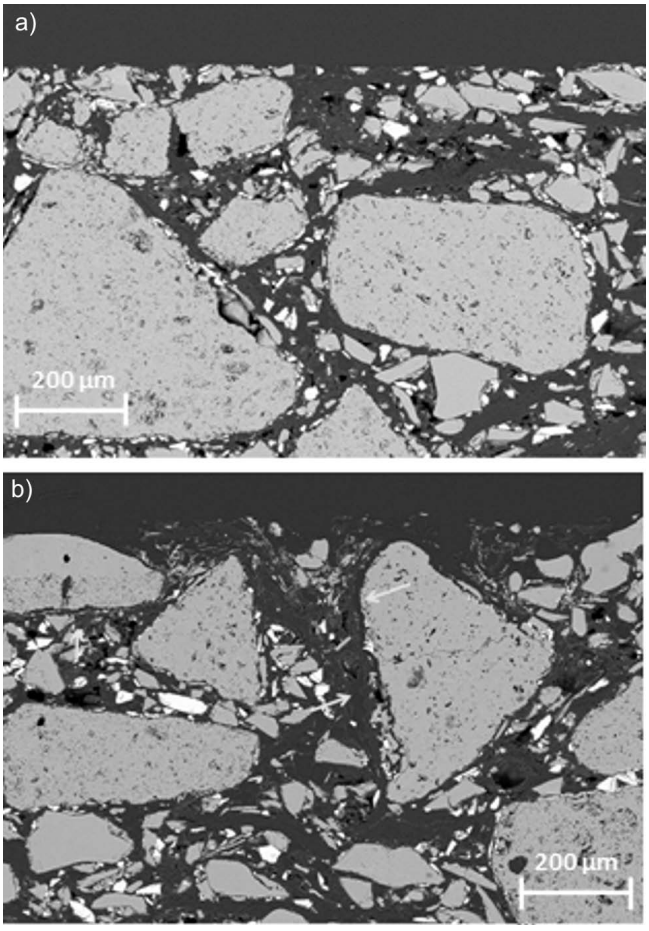

Fig. 13: a) SEM-image of an undamaged Al_2O_3-C sample; b) SEM-image of an Al_2O_3-C sample after thermal shocked with condition 3.

IV. Summary and Conclusions

In the current study, the thermo-mechanical behavior of different carbon-reduced and carbon-free refractories for steel applications was investigated with novel and improved testing methods. An optimized WST for small sample geometries was carried out with different loading configurations. LC1 does not yield reproducible load-displacement curves for any material as verified for alumina. With LC2, stable load-displacement curves were obtained for both tested materials (alumina and Al_2O_3-C). An additional advantage of LC2 is that the friction coefficient appears to be material-independent, whereas a friction coefficient for LC1 has to be obtained for each investigated material. However, sample preparation for LC1 is less complex. Overall, the necessary loading configuration of WST should be adapted to the expected and obtained material properties.

A strong size effect for the obtained work of fracture was found for alumina materials, while Al_2O_3 and AZT materials as well as Al_2O_3-C materials did not reveal a clear size effect. A size effect of work of fracture occurs for materials that display an *R*-curve behavior: The crack resistance (dissipated energy/crack extension) or fracture toughness increases with increasing crack propagation owing to toughening effects in the wake region. A plateau value is reached when the formation of the wake zone is completed. For a sufficiently long crack, the work of fracture becomes constant. The absence of a size effect for Al_2O_3-C can be explained with its significantly smaller maximum grain size compared to the alumina materials (0.6 vs. 1 mm). Considering only this effect, a grain size reduction leads to lower roughness of the fracture surface and therefore to a smaller wake zone. However, Al_2O_3 and AZT materials do not reveal a clear size effect, while having the same maximum grain as the alumina materials. One of the differences between the materials is the very weak grain bonding behavior of alumina materials. It can be assumed that large alumina grains are pulled out the matrix during crack opening, this effect would lead to an increase of the fracture surface roughness and the wake region.

In addition to the widely discussed microstructural development of AZT at RT [20, 29, 30], elevated temperature investigations revealed a huge effect of the ZrO_2 phase transition on mechanical properties. Experiments up to 1000 °C showed more brittle behavior than at RT. However, the formation of Al_2TiO_5 and its accompanied volume expansion of 11 vol% is expected to have an influence on the microstructure at temperatures > 1280 °C and hence might have a crucial impact on thermomechanical behavior in operation conditions.

Thermal shock tests with the JUDITH 1 electron beam facility were carried out with Al_2O_3-C materials. This method requires electric conductivity of the tested sample and can be used to apply severe thermal shock to carbon-containing refractory materials. No significant differences could be observed in the damage of the different Al_2O_3-C materials. Compared to initial investigations by Skiera *et al.* [20] and Böhm [23] on MgO-C materials, a more homogenous damage pattern was observed for the thermal shock test with the JUDITH 1 electron beam facility than for experiments carried out previously at the JUDITH 2 electron beam facility [13]. A main difference is that lower ero-

sion effects are obtained for the same power densities. One reason might be the different shape of the electron beam (3 mm diameter in the case of JUDITH 2 and 1 mm diameter for JUDITH 1) or the different relation of acceleration voltage to beam current (40 kV and 500 mA in JUDITH 2 experiments compared to 120 kV and 78 – 165 mA in JUDITH 1). These differences are constrained by the boundary conditions of the machine parameters and cannot be varied in a wide range.

Acknowledgement

The funding of the present work by the German Research Association (DFG) under the DFG grant MA 5757/1 – 2 is gratefully acknowledged. In addition, the authors would like to thank Mr J. Mönch and Ms T. Osipova for technical support, Dr E. Wessel for SEM investigations and Mr M. Ziegner for carrying out XRD experiments.

References

1 Lee, W.E., Moore, R.E.: Evolution of *in situ* refractories in the 20th century, *J. Am. Ceram. Soc.*, **81**, [6], 1385 – 1410, (1998).

2 Harmuth, H.: Fracture mechanics characterization of heavy clay refractory materials – importance, procedure and application, (in German), *Ber. Dt. Keram. Ges.*, **10**, [3], 27 – 61, (1994).

3 Hasselman, D.P.H.: Unified theory of thermal shock fracture initiation and crack propagation in brittle ceramics, *J. Am. Ceram. Soc.*, **52**, [11], 600 – 604, (1969).

4 Hasselman, D.P.H.: Thermal stress resistance parameters for brittle refractory ceramics – a compendium, *Am. Ceram. Soc. Bull.*, **49**, [12], 1033 – 1037, (1970).

5 Tschegg, E.K., Linsbauer, H.: Test set-up for determination of fracture mechanics characteristics as well as test specimens suitable for this, (in German), Austrian Patent, (1989).

6 Tschegg, E.K.: New equipment for fracture tests on concrete, *Materialprüfung*, **33**, [11 – 12], 338 – 343, (1991).

7 Harmuth, H., Tschegg, E.K.: A fracture mechanics approach for the development of refractory materials with reduced brittleness, *Fatigue Fract. Eng. M.*, **20**, [11], 1585 – 1603, (1997).

8 Ribeiro, S., Rodrigues, J.: The influence of microstructure on the maximum load and fracture energy of refractory castables, *Ceram. Int.*, **36**, [19], 263 – 274, (2010).

9 Kim, J.K., Kim, Y.Y.: Fatigue crack growth of high-strength concrete in wedge-splitting test, *Cement Concrete Res.*, **29**, [5], 705 – 712 (1999).

10 DIN EN 820 – 3: Advanced technical ceramics – methods of testing monolithic ceramics – thermomechanical properties – Part 3: determination of resistance to thermal shock by water quenching, 2004.

11 Linke, J., Bolt, H., Doerner, R., Grübmeier, H., Hirooka, Y., Hoven, H., Mingam, C.: Performance of boron/carbon first wall materials under fusion relevant conditions, *J. Nucl. Mater.*, **176**, 856 – 863, (1990).

12 Hirai, T., Kreter, A., Linke, J., Malzbender, J., Ohgo, T., Philipps, V., Pintsuk, G., Pospieszczyk, A., Sakawa, Y., Sergienko, G., Tanabe, T., Ueda, Y., Wada, M.: Critical heat flux loading experiments on CVD-W coating in the TEXTOR tokamak, *Fusion Eng. Des.*, **81**, 175 – 180, (2006).

13 Skiera, E., Thomser, C., Linke, J., Roungos, V., Aneziris, C.G.: Thermal shock testing of different carbon bonded MgO-C materials by application of an electron beam test facility, *Refractories Worldforum*, **4**, [1], 125 – 129, (2012).

14 Aneziris, C.G., Dudczig, S., Gerlach, N., Berek, H., Veres, D.: Thermal shock performance of fine-grained Al_2O_3 ceramics with TiO_2 and ZrO_2 additions for refractory applications, *Adv. Eng. Mater.*, **12**, [6], 478 – 485, (2010).

15 Aneziris, C.G., Pfaff, E., Maier, H.: Ceramic materials in the system ZrO_2-TiO_2-Al_2O_3 for applications in the ferrous and non ferrous metallurgy, *Key Eng. Mater.*, **132**, 1829 – 1833, (1997).

16 Aneziris, C., Schärfl, W., Ullrich, B.: Microstructure evaluation of Al_2O_3 ceramics with Mg-PSZ- and TiO_2-additions, *J. Eur. Ceram. Soc.*, **27**, [10], 3191 – 3199, (2007).

17 Stein, V., Aneziris, C.: Low-carbon carbon-bonded alumina refractories for functional components in steel technology, *J. Ceram. Sci. Tech.*, **5**, [2], 115 – 124, (2014).

18 Aneziris, C.G., Klippel, U., Schärfl, W., Stein, V., Li, Y.: Functional refractory material design for advanced thermal shock performance due to titania additions, *Int. J. Appl. Ceram. Tec.*, **4**, [6], 481 – 489, (2007).

19 Roungos, V., Aneziris, C., Berek, H., Skiera, E., Thomser, C.: Advances of nanoscaled additives on the thermo-mechanical performance of Al_2O_3-C and MgO-C refractories, *Refractories Worldforum*, **4**, [1], 91 – 104, (2012).

20 Skiera, E., Malzbender, J., Mönch, J., Dudczig, S., Aneziris, C.G., Steinbrech, R.W.: Controlled crack propagation experiments with a novel alumina-based refractory, *Adv. Eng. Mater.*, **14**, [4], 248 – 254, (2012).

21 Böhm, A., Fruhstorfer, J., Mertke, A., Aneziris, C.G., Malzbender, J.: Thermal shock behavior of carbon reduced refractories. in: proceedings of the unified international technical conference on refractories. Victoria, Canada, 2015.

22 Mertke, A., Aneziris, C.: The influence of nanoparticles and functional metallic additions on the thermal shock resistance of carbon bonded alumina refractories, *Ceram. Int.*, **41**, [1], 1541 – 1552, (2015).

23 Böhm, A.: Thermal shock behavior and temperature-dependent properties of carbon-reduced and carbon-free refractory materials, Ph.D. thesis, RWTH Aachen, (2015).

24 DIN 51045: Determination of linear thermal expansion of solids, 2005.

25 Wei, J., Pecanac, G., Malzbender, J.: Review of mechanical characterization methods for ceramics used in energy technologies, *Ceramic Int.*, **40**, [10], 15371 – 15380 (2014).

26 Malzbender, J., Steinbrech, R.W., Singheiser, L.: A review of advanced techniques for characterising behaviour, *Fuel Cells*, **9**, [6], 785 – 793, (2009).

27 ASTM E 1876 – 01: Standard test method for dynamic young's modulus, shear modulus, and poisson's ratio by impulse excitation of vibration, 2005.

28 Skiera, E.: Thermomechanical characterization of newly developed refractory materials, Ph.D. thesis, RWTH Aachen, (2012).

29 Aneziris, C., Schär, W., Ullrich, B.: Microstructure evaluation of Al_2O_3 ceramics with Mg- PSZ- and TiO_2-additions, *J. Eur. Ceram. Soc.*, **27**, [10], 3191 – 3199, (2007).

30 Aneziris, C.G., Dudczig, S., Gerlach, N., Berek, H., Veres, D.: Thermal shock performance of fine-grained Al_2O_3 ceramics with TiO_2 and ZrO_2 additions for refractory applications, *Adv. Eng. Mater.*, **12**, [6], 478 – 485, (2010).

31 Fruhstorfer, J., Möhmel, S., Thalheim, M., Schmidt, G., Aneziris, C.G.: Microstructure and strength of fused high alumina materials with 2.5 wt% zirconia and 2.5 wt% titania additions for refractory applications, *Ceram. Int.*, **41**, [9], 10644 – 10653, (2015).

32 Michalowsky, L., Hermann, M.: New ceramic materials, (in German), Wiley Online Library, (1994).

[33] Pandolfelli, V., Rodrigues, J., Stevens, R.: Effects of TiO_2 addition on the sintering of ZrO_2 – TiO_2 compositions and on the retention of the tetragonal phase of zirconia at room temperature, *J. Mater. Sci.*, **26**, 5327 – 5334, (1991).

[34] Gault, C., Platon, F. and Bras, D.L.: Ultrasonic measurements of Young's modulus of Al_2O_3-based refractories at high temperatures, *Mater. Sci. Eng.*, **74**, [1], 105 – 111, (1985).

[35] Traon, N., Etzold, S., Tonnesen, T., Telle, R.: Influence of zirconia doping agent on the fatigue of high alumina refractory castables at elevated temperatures, In: Proceedings of the Unified International Technical Conference on Refractories. Victoria, Canada, 2015.

[36] Joliff, Y., Absi, J., Huger, M., Glandus J.C.: Experimental and numerical study of the elastic modulus vs. temperature of debonded model materials, *Comp. Mater. Sci.*, **44**, [2], 826 – 831, (2008).

[37] Kuchling, H.: Physics Pocket Book, (in German), 20th Edition, München, Fachbuchverlag Leipzig, (2011).